

# Remote and low-cost intraocular pressure monitoring by deep learning of speckle patterns

Zeev Kalyuzhner (✉ [zeevkal@biu.ac.il](mailto:zeevkal@biu.ac.il))

Bar Ilan University

Sergey Agdarov

Bar Ilan University

Yevgeny Beiderman

Holon Institute of Technology

Aviya Bennett

Bar Ilan University

Yafim Beiderman

Bar Ilan University

Zeev Zalevsky

Bar Ilan University

---

## Article

### Keywords:

**Posted Date:** November 22nd, 2022

**DOI:** <https://doi.org/10.21203/rs.3.rs-2277668/v1>

**License:**   This work is licensed under a Creative Commons Attribution 4.0 International License.

[Read Full License](#)

**Additional Declarations:** No competing interests reported.

---

# Remote and low-cost intraocular pressure monitoring by deep learning of speckle patterns

Zeev Kalyuzhner <sup>1\*</sup>, Sergey Agdarov <sup>1</sup>, Yevgeni Beiderman <sup>2</sup>, Aviya Bennet <sup>1</sup>, Yafim Beiderman <sup>1</sup> and Zeev Zalevsky <sup>1</sup>

<sup>1</sup>Faculty of Engineering and the Nanotechnology Center, Bar-Ilan University, Ramat-Gan, 5290002, Israel

<sup>2</sup>Faculty of Electrical Engineering, Holon Institute of Technology (HIT), Holon 5810201, P.O.B 305, Israel.

## Abstract

Intraocular pressure (IOP) measurements comprise an essential tool in modern medicine for the early diagnosis of glaucoma, the second leading cause of human blindness. The world's highest prevalence of glaucoma is in low-income countries.

Current diagnostic methods require experience in running expensive equipment as well as the use of anesthetic eye drops. We present herein a remote photonic IOP bimonitoring method based on deep learning of secondary speckle patterns, captured by a fast camera, that are reflected from eye sclera stimulated by an external sound wave. By combining speckle pattern analysis with deep learning, high precision measurements are possible.

The method was tested under artificially varying eye pressures on a series of 24 pig eyeballs, found to be similar to human eyes.

As a low-cost procedure, it has the potential to meet clinical needs in low- and middle-income countries and at points of care everywhere.

# 1. Introduction

Glaucoma is a major source of irreversible blindness and the second leading cause of the condition, resulting in a global burden on a massive scale, especially in developing countries<sup>1-6</sup>. The disease is characterized by a series of progressive optic neuropathies, defined by the deterioration of retinal ganglion cells and retinal nerve fiber layers, causing abnormalities in the optical nerve head<sup>1,5</sup>. High intraocular pressure (IOP) caused by the disease leads to optic nerve degeneration and the death of the retinal ganglion cells<sup>7-10</sup>.

Glaucoma comes in a variety of forms. Of these, open-angle glaucoma (OAG), normal tension glaucoma, angle-closure glaucoma (ACG), pigmentary glaucoma, and trauma-related glaucoma are the most prevalent<sup>8,11-15</sup>. However, the distinction between normal tension glaucoma under normal IOP and ocular hypertension with higher IOP without causing the illness remains unclear<sup>13-15</sup>.

IOP is a dynamic physiologic factor having regular circadian and random variations over short and extended periods as the subject's muscular tone and physiologic state alternate<sup>11-14,16-18</sup>. Reliable IOP monitoring is thus a critical clinical element in glaucoma management. Although many healthcare glaucoma-related decisions are based on IOP, contemporary glaucoma treatments include frequent IOP assessments during office hours. However, this is a poor resolution that provides inadequate definition of the IOP's fluctuating nature<sup>12,19</sup>.

Goldmann applanation tonometry (GAT) is the most extensively used ophthalmic tool for measuring IOP<sup>20-22</sup>. Although GAT is precise, it is influenced by inner-individual variances owing to differences in corneal thickness and stiffness<sup>22</sup>. The method is intrusive and necessitates administration of anesthetic eye drops, limiting IOP monitoring over time. Biochemical features of the cornea affect the accuracy of the applanation tonometry. The ocular response analyzer (ORA) allows IOP adjustment by considering the biomechanical parameters of the cornea<sup>21-24</sup>. By directing an ultrasonic wave to the surface of the eye, researchers have been able to evaluate biological pulses, blood flow<sup>25</sup> and mechanical resonance modes

of the eye cornea under sound wave stimulation<sup>26</sup>. Despite the fact that such procedures employ sound-driven technology to measure the physical properties of the eyes, no association with IOP has been found<sup>19,27</sup>. An alternative method of IOP measurement is based on the air puff tonometer, which evaluates IOP based on the resistance of the eye to the air puff<sup>28</sup>. However, over long periods, in order to get full IOP profiles, the method is not suitable.

This above constraint has triggered the need to devise novel ways for continuous IOP monitoring. Several reported examples include implantable telemetric pressure transducers<sup>29–32</sup>, sensing contact lenses<sup>15,33–37</sup>, implantable microfluidic devices<sup>38</sup>, ocular telemetry sensors<sup>39</sup>, and optical devices<sup>40–43</sup>.

A particular laser-based system has demonstrated the capacity to remotely recognize speech signals<sup>44</sup>, heart beats<sup>44</sup>, blood pulse pressure<sup>45,46</sup>, blood oxygen saturation<sup>47</sup> and sensations<sup>48,49</sup>. A former method<sup>50</sup> involved remote evaluation of IOP based on the speckle pattern analyses of sound wave–stimulated fisheye samples. The method evaluates IOP by analyzing the damping factor of sclera-free oscillations<sup>50</sup>.

We propose remote photonic IOP biomonitoring based on temporally encoded external sound wave stimulation, which does not require direct contact with the eye and is inexpensive to build. The suggested configuration includes projection of a laser beam on eye sclera stimulated by a sound wave, and recording of the scattered speckle patterns by a fast-imaging camera. In order to forecast and effectively reduce background noise from the recorded signal, we created a deep learning driven IOP measurement model. This model allows deep analysis of the recorded signal, considering not only free eye sclera oscillation, but also forced oscillation under periodic stimulation.

The method was successfully tested on 24 pig eyeball samples, given their similarity to the human eye<sup>51,52</sup>. The tests were conducted by artificial variation of IOP. High detection capacity was achieved without preliminary calibration.

## 2. Results

### 2.1 IOP biomonitoring system setup

We demonstrated the technical feasibility of a new remote, cost-effective IOP monitoring technology by designing and constructing a system that comprises a 532 nm green laser illuminating the eye sclera, and a Basler AcaA1300-200um area scan camera with defocused optics to capture the reflected speckle patterns. A needle inserted into the rear side of the eye controlled the IOP of the pig eye sample. The needle was connected to a calibrated burette filled with water. The sound wave source agitating the sclera was connected to a frequency generator. A computer using a MATLAB-based image cross correlation program, as shown in Fig. 1, refined the video files recorded by the camera. The external signal extracted from the sound wave sclera stimulation was analyzed by a developed deep learning algorithm.

### 2.2 Results of the generic IOP classification method

Generic remote IOP classification does not require any prior knowledge and the model predicts the IOP accurately. Classification of the speckle patterns and their association with a specific IOP level was carried out using a deep neural network (DNN). The results of the validation are given in Table 1, showing that our model achieved an accuracy of 91%. Fig. 2(a) displays a confusion matrix of the trained generic model and a 100-millisecond data sample of pre-processed pig eye speckle pattern displacement. The confusion matrix shows that IOP detection of a single test sample within the normal range is 97%, with a low error rate. The success rates for identifying high IOP ranges are also high and stand at 84% (22-33 mm Hg) and 70% (34-45 mm Hg), with almost all errors between 84% and 97%. The data plot presented in Table 1 shows a sample of the three IOP ranges classified by the generic model, each range marked by a different color.

Table 1 shows that under the normal IOP range the amplitude variations are usually smaller than for the two high IOP ranges. The variance between the amplitudes for the different IOP ranges indicates that our definition of the IOP classification problem is accurate and that our suggested method is both sound and feasible.

### 2.3 IOP classification for a particular pig eye

The specific eye classification task component permits more precise estimation of IOP and a higher resolution. Using calibration and prior knowledge of the specific eye, this approach identifies each eye uniquely. The measurement procedures classify IOP sensitivity into three classes: 5-, 3- and 1-mm Hg. Table 1 shows the average of our measurement metrics for all IOP ranges in the 24 tested eyes – these being precision, recall and accuracy.

The 5-mm Hg measurement step was applied to two classes: 10-15 mm Hg, and 16-21 mm Hg. The accuracy of identifying IOP for each range is about 80%. The second IOP classification for the individual eye maintained a 3-mm Hg step and shows an accuracy of 83%. Table 1 shows that the high values of the measurement metrics occur at the edges of the IOP ranges, i.e. 10-13 mm Hg, giving an F1 score of 84%, and under 18-21 mm Hg, with an F1 score of 87%, similar to the classification under the 1-mm Hg IOP step. Within the 10-11 mm Hg IOP range, model precision reached 82%, while for the 20-21 mm Hg IOP range it is 86%.

Fig. 2(b) displays the confusion matrices of the three mentioned IOP classification tasks. It shows that the trained IOP classification model errors are common for the near IOP ranges and are not dispersed across all possible IOP ranges, indicating the effective learning process of the model. In addition, the confusion matrix for the 1-mm Hg IOP step variation shows that the high error rate occurs in the middle IOP ranges and not at the edges. The values of these errors are also relatively low.

## 2.4 Explanation of IOP classification model results

The DNN models were optimized during the training process. Our DNN networks are based on 1D convolutional layers, which are found useful for the IOP classification tasks due to their weight sharing, sparsity of connection capabilities, parameter efficiency, and other factors. Another main feature of the convolutional layers is the feature extractor. Extracting our trained convolutional layer filters by displaying them on a new input signal, as can be seen in Fig. 4(a), allows an understanding to be gained of the behavior of the model's decision-making process. As shown in Fig. 4(b) and 4(c), the input signal has a duration of 25,000 milliseconds and is normalized in the range of (0, 1) to represent 26 consecutive cycles. In addition, Fig. 4(b) shows our trained 64 convolutional layer filters, and the final convolutional layer of the DNN, with the corresponding amplitude expressing the confidence level of the decision, where 1 indicates the highest degree and 0 the lowest. Fig. 4(c) demonstrates that the proposed DNN classifies the IOP level when the eyeball starts or stops reacting to the sound of the external stimulation signal, defined by the periodic vibratory profile. Each IOP level involves variation of the eye weight, volume, and geometry, which in turn has a direct impact on the eye shape, direction, and speed of movement influenced by the agitating sound wave. It is reasonable to conclude from the physiological explanation that by remote sensing micro-vibrations of the eye, induced by an external sound signal, the IOP level of the eye can be determined.

### 3. Discussion

The current methods for IOP measurement, such as GAT and ORA, require significant resources, expensive equipment, and close proximity or physical contact with a patient<sup>20–24,33</sup>. In this study, we developed and demonstrated low-cost, remote photonic IOP biomonitoring. The method applies DNN classification of speckle patterns reflected from eye sclera illuminated by a laser beam when temporally encoded external sound wave stimulation is applied. Such a noncontact biomonitoring tool is relatively inexpensive in terms of manufacture and operation. For mass manufacture, we estimate hardware material costs of under US\$ 5,000. The device can be made compact, is potentially mobile, and is highly accurate even without preliminary calibration or preliminary information on the tested eye. We succeeded in IOP biomonitoring of 24 eyes of a living creature having characteristics that are closest to the human eye<sup>51,52</sup>, demonstrating high IOP measurement accuracy and potential clinical utility.

#### 3.1 Potential benefits of photonic-based remote IOP monitoring

The high cost of procuring, installing, maintaining, and operating the current clinical IOP measurement devices constitutes a major roadblock in IOP diagnostics<sup>22,23</sup>. Our low-cost, compact, remote photonic-based diagnostic tool for IOP biomonitoring aims to complement rather than compete with existing high-performance clinical IOP measurement devices.

GAT, the most used ophthalmic instrument tool for IOP examination<sup>20,22,33</sup>, is very accurate, but is affected by individual variations due to diversity in corneal thickness and rigidity, while being an invasive procedure that necessitates the use of anesthetic eye drops, limiting IOP monitoring over time<sup>22</sup>. We propose a configuration which includes projection on the eye sclera of an eye-safe laser beam (with a power level of 750 $\mu$ W as per European standard EN 60825-1) and observation by a fast-imaging camera of scattered secondary speckle patterns after being temporally encoded by a sound wave used as an external

stimulation signal. Our photonic-based system offers an accurate non-invasive diagnostic IOP measuring tool.

To simulate the IOP, an injection needle inserted in the eyeball was connected to a calibrated burette filled with water by means of a flexible pipe. Each 1 mm Hg was considered equivalent to a 13.2 mm water column (Fig. 3). Each eye was tested under a single needle penetration and the IOP was increased in steps of 1 mm Hg in the range of 10-45 mm Hg in order to obtain high accuracy in the normative pressure range. This ability to create a ground truth renders the data collection process effective for the model training process while ensuring reliable results.

The results of the generic IOP model show an accuracy of over 90% with near-perfect normative IOP detection. The system can be useful in early detection of glaucoma. The eyes identified as having high IOP can be monitored by an accurate personal IOP measurement system.

For the purpose of demonstrating the feasibility of our method, pig eyes, which are remarkably similar to human eyes, were employed to provide a reliable data collection process with accurate ground truth, and to simulate clinically significant human glaucoma<sup>51,52</sup>.

### **3.2 Challenges of photonic-based remote IOP monitoring**

Data was collected from 24 pig eyeballs tested in a controlled environment. The laboratory was darkened and silenced to avoid background noises that could affect the installed system<sup>49</sup>.

In inserting the needle into the eyeball, we controlled the direction of insertion without validating the exact location inside the eye. Since the eyeball constitutes living tissue, it may be reasonably assumed that several needles experienced partial blockage, perhaps affecting the reference IOP. Such blockage could possibly explain the error rate, which increases between close IOP ranges since the sensitivity threshold of the system is limited.

## 4. Method

### 4.1 IOP biomonitoring system design

The pig eye has become a popular research model due to the ethical and financial constraints involved in employing eyes of other species<sup>51,52</sup>. Pig eyes are very similar to human eyes, having holangiotic retinal vasculature, no tapetum, cone photoreceptors in the outer retina, and similar scleral thickness<sup>53</sup>.

The 24 tested pig eyeballs were acquired from a local distributor within less than two hours postmortem, and experiments were performed within eight hours following delivery. The eyeballs were fixed with 4% paraformaldehyde in 0.1 M phosphate buffer saline (PBS, pH 7.4) for four hours at 4°C, subsequent to which the retinas were removed and flat-mounted with the retinal ganglion cell layer uppermost. They were then cover-slipped with PBS/glycerin (1:1).

The optically based monitoring device was positioned at a distance of 35 cm from the tested pig eyeball. Since diffraction of the speckle occurs over a wide angle<sup>44</sup>, no constraint exists concerning the position of the fast-imaging camera. A 532 nm green laser was positioned directly opposite the illuminated eyeball Fig. 1(a). The laser beam, covering a 3 mm diameter area, was fixed at a selected location of the sclera adjacent to the pupil. The 750 $\mu$ W laser power was considered safe for human eyes<sup>54</sup>. Speckle patterns reflected from the eye sclera were recorded using a Basler Aca1300-200 nm digital camera set for 1,000 frames per second (FPS), with a spatial resolution of 64 $\times$ 64 pixels. The camera's focal length was 55 mm, with an F-number of 2.8. The camera was focused on the far field, defocusing the sclera and the speckle pattern. Defocusing caused the speckle pattern to move only in the transversal plane. For stimulation of the sclera, we used a high-fidelity loudspeaker (Pioneer Ts-G1615R) with an excitation frequency of 390Hz@105dB<sup>50</sup>, found to be highly responsive (after a sweep on frequencies between 130 and 1000 Hz). An arbitrary waveform function generator (Tektronix, AFG3022B) controlled the speaker, as shown in Fig. 1(b). For each recording, the sound wave agitated the pig eye by 26 consecutive cycles, each cycle

comprising one second of stimulation followed by one second of a break. The frame rate of the digital camera was more than twice the stimulation frequency in order to meet the Nyquist ratio requirements. Each frame of the camera output contained a secondary speckle pattern.

The stimulated eye pressure was measured in millimeters of mercury (mm Hg) and normal eye pressure set in the range of 10-21 mm Hg<sup>6</sup>. Each 1 mm Hg was considered equivalent to a 13.2 mm water column (Fig. 3). Each eye was tested by a single needle penetration and the IOP was set for each 1 mm Hg in the range of 10-45 mm Hg in order to obtain high accuracy in the normative pressure range. Above a pressure of 21 mm Hg, testing was performed with 2 mm Hg steps. The top IOP value was set at 45 mm Hg. Each tested eye was rejected after complete testing within one day under singular needle penetration.

## 4.2 Data processing

Tests were conducted on separate dates upon receipt of the samples, and each pig eyeball was tested in one continuous session. The dataset contained roughly 20 million frames. Each pig eyeball video was given a unique identification consisting of the duration of measurement and the IOP reference value<sup>49</sup>.

The videos from different recording days were subdivided into training and test datasets prior to subdivision into specific frames. Data for all tested eyeballs was included in the training and test sets, preventing any mixing between the two sets, which could have occurred with a simple random split<sup>48</sup>.

IOP classification was divided into two testing components. The first component determined IOP in a discrete manner, requiring no calibration or prior knowledge about the tested eye. The main goal of this component was to identify abnormal IOP levels for further examination. The classification system subdivided the input signal into one of three possible classes with a range of 12 mm Hg. The first class was the normal range of 10-21 mm Hg. The second class, 22-33 mm Hg, represented the high IOP range. The third class, 34-45 mm Hg, represented the extremely high IOP range.

The second component determined the IOP of each tested eye with an accuracy level of 1 mm Hg, requiring prior calibration. The process involves training a model for each individual. To prove the

feasibility of the method, we focused on the normal IOP range of 10-21 mm Hg. A set of IOP sensitivity techniques was defined such that each successive technique improved accuracy over its predecessor. The first technique was a binary classification task that classified two IOP ranges: 10-15 mm Hg and 16-21 mm Hg, each having a 6 mm Hg range. The second technique was able to classify three different IOP ranges: 10-13 mm Hg, 14-17 mm Hg and 18-21 mm Hg. The latter technique was able to classify the exact measured IOP level with a deviation range of 1 mm. Each model was tested for each eyeball and compared with all tested eyeballs.

The generic and individual components of IOP monitoring allowed design of an IOP classification system that is accurate and general, permitting rapid identification of both abnormal and normal IOP.

In order to classify the IOP, each video, containing 52,000 frames, was pre-processed for frame correlation extraction (Fig. 3). For every two consecutive frames, the correlation was calculated using a full discrete 2-dimensional linear cross-correlation<sup>55</sup> with symmetrical boundary conditions, representing the shift between the two consecutive frames. This signal was normalized using the Manhattan norm<sup>56</sup> as in Eq. 1 below.

$$norm = \sum_{i=1}^n |diff_{(i,i+1)}| \quad (1)$$

Where  $diff$  is the correlation between two consecutive frames and label for sample  $i$ .

As part of the output, a one-dimensional array was created by pre-processing all the frames of each recorded video. Quantitative assessment and comparison of our proposed method used the metrics shown in Eq. 3-6, where TP = True Positive; TN = True Negative; FP = False Positive; and FN = False Negative, calculated pixelwise by the logical operators given in Eq. 2.

$$\begin{aligned} TP_i &= (x_i == 1) \& (y_i == 1) & \quad TN_i &= (x_i == 0) \& (y_i == 0) \\ FP_i &= (x_i == 1) \& (y_i == 0) & \quad FN_i &= (x_i == 0) \& (y_i == 1) \end{aligned} \quad (2)$$

$$accuracy = \frac{1}{n} \sum_{i=1}^n \frac{TP_i + TN_i}{TP_i + TN_i + FP_i + FN_i} \quad (3)$$

$$precision = \frac{1}{n} \sum_{i=1}^n \frac{TP_i}{TP_i + FP_i} \quad (4)$$

$$recall = \frac{1}{n} \sum_{i=1}^n \frac{TP_i}{TP_i + FN_i} \quad (5)$$

$$F_1 = \frac{1}{n} \sum_{i=1}^n \frac{2TP_i}{2TP_i + FN_i + FP_i} \quad (6)$$

The tuple  $(x_i, y_i)$  is the model prediction and the label for sample  $i$ .

It is important to note that all experiments were carried out in accordance with existing guidelines and regulations. Although deconstructed for laboratory optimization purposes, the device is entirely laser- and tissue-safe, as previously obtained from international regulators.

### 4.3. Deep learning for IOP classification

The model input data for IOP classification is a vector containing cross-correlation peaks of the recorded consecutive video frames. This data was used to train a four-layer DNN model for IOP classification. The data was divided into training and testing sets, as explained in the previous section. The model was then applied separately to each of the three techniques for IOP classification.

The model output depended on the specific technique. The first three layers within the DNN model were a combination of 1D convolution<sup>57</sup>, batch normalization<sup>58</sup> and rectified linear unit (ReLU)<sup>59</sup>, followed by a global average pooling operation<sup>60,61</sup>. The last layer was a regular densely connected NN layer with a SoftMax activation function<sup>62</sup>. The kernel size of each 1D convolutional layer was 3, with the corresponding number of filters being 64. The output of the network, representing the IOP classification resolution, depended on the specific IOP sensitivity technique.

The loss function was categorical cross entropy<sup>63</sup>. During training, the loss was minimized using the Adam optimizer<sup>64</sup> with  $\beta_1 = 0.9$ ,  $\beta_2 = 0.999$  and initial learning rate = 0.001. Using the Reduce Learning-Rate on Plateau callback<sup>65</sup>, we reduced the learning rate when the validation loss stopped improving.

This deep learning procedure was implemented with a batch size of 32 for 500 epochs on a single 1080Ti graphics processing unit (GPU) using a TensorFlow package.

#### 4.4. Comparison between the remote photonic validation method and the prior method

The prior method for remote laser speckle-based IOP biomonitoring evaluates the intraocular pressure by calculating the damping (Q) factor of transitional oscillations occurring on the surface of eye sclera after terminating its stimulation by a temporally encoded sound wave<sup>50</sup>. This methodology was tested on artificial eyes as well as on fisheyes. We chose a set of 24 pig eyes for testing for two reasons: they represent a suitable animal model for glaucoma research due to the similarities between the pig eye and the human eye when subjected to chronically increased intraocular pressure; and there is a greater availability of pig eyes compared to nonhuman primate eyes<sup>51,52</sup>.

However, whereas the prior method requires preliminary calibration to improve measurement precision, our method can classify different IOP ranges without any prior calibration or knowledge regarding the IOP level of the eye. In addition to the Q factor, the prior method analyzed only the dumping part of the cornea vibration, while part of the information related to forced agitation was not analyzed. Our method analyzes the entire signal, which contains more robust data, increasing the classification rate accuracy.

## 5. Conclusions

We developed a photonic IOP biomonitoring system using DNN analysis of remotely recorded speckle pattern signal data. The method is completely contact-free, low-cost, and mobile. We succeeded in performing high IOP detection accuracy on 24 pig eyeballs using this hardware and software platform. The preliminary clinical feasibility of diagnosing high IOP, the cause of glaucoma, was demonstrated. Development of such photonic-based technology will enable unmet clinical needs across various global

healthcare sites to be fulfilled, having the potential to democratize IOP diagnosis for low- and middle-income countries.

## Corresponding Author

Zeev Kalyuzhner: zeevkal@biu.ac.il

## Author contributions

Z.K. created the models and conducted the training. All authors contributed to the design of the study, conducting the tests, interpreting the results, and writing the manuscript.

## Competing interests statement

The authors declare no competing interests.

## Data availability statement

The data generated to support the findings of this study is available from the corresponding author upon reasonable request.

## Code availability statement

The code is available at <https://github.com/zeevikal/iop-speckle>.

## References

1. Quigley, H. A. Number of people with glaucoma worldwide. *British Journal of Ophthalmology* **80**, 389–393 (1996).
2. Spaeth, G. L. *A New Classification of Glaucoma Including Focal Glaucoma*. *Goldberg Glaucoma Service and Resen* vol. 38 (1994).
3. MayoClinic.org. Mayo Clinic. <http://www.mayoclinic.org/> (2016).
4. Nei.nih.gov. National Eye Institute. *Nei.nih.gov*.
5. Lee, D. A., of, D. & Higginbotham, E. J. *CLINICAL REVIEW Glaucoma C L I N I C A L R E V I E W Glaucoma and its treatment: A review*. *Am J Health-Syst Pharm*.
6. Glaucoma.org. Glaucoma Research Foundation | Treatment, Education, Information, Research Progress. (2018).
7. Glaucomafoundation.org. Glaucoma Research, Information, and Education. (2018).

8. Kass, M. A. *et al.* *The Ocular Hypertension Treatment Study A Randomized Trial Determines That Topical Ocular Hypotensive Medication Delays or Prevents the Onset of Primary Open-Angle Glaucoma.* www.vrcc.wustl.edu,.
9. Lichter, P. R. *et al.* *Interim Clinical Outcomes in The Collaborative Initial Glaucoma Treatment Study Comparing Initial Treatment Randomized to Medications or Surgery.* (2001).
10. Cristina Leske, M. *et al.* *Factors for Glaucoma Progression and the Effect of Treatment The Early Manifest Glaucoma Trial.* *Arch Ophthalmol* vol. 121 <https://jamanetwork.com/> (2003).
11. Srinivasan, S. *et al.* Diurnal intraocular pressure fluctuation and its risk factors in angle-closure and open-angle glaucoma. *Eye (Basingstoke)* **30**, 362–368 (2016).
12. Konstas, A. G. P., Mantziris, D. A., Cate, E. A. & Stewart, W. C. *Effect of Timolol on the Diurnal Intraocular Pressure in Exfoliation and Primary Open-angle Glaucoma Conclusion: Despite a greater initial IOP reduction in the patients with EXG treated with timolol, a higher IOP and significant fluctuation in the diurnal curve of IOP during the time in which patients received therapy still characterized EXG from POAG.* <http://archophth.jamanetwork.com/>.
13. Drance, S. M. *Comparison of Glaucomatous Progression Between Untreated Patients With Normal-Tension Glaucoma and Patients With Therapeutically Reduced Intraocular Pressures COLLABORATIVE NORMAL-TENSION GLAUCOMA STUDY GROUP\*.* (1998).
14. Drance, S. M. *The Significance of the Diurnal Tension Variations in Normal and Glaucomatous Eyes.* <http://archophth.jamanetwork.com/>.
15. Agnifili, L. *et al.* Circadian intraocular pressure patterns in healthy subjects, primary open angle and normal tension glaucoma patients with a contact lens sensor. *Acta Ophthalmologica* **93**, e14–e21 (2015).
16. Ericson, L. A. TWENTY-FOUR HOURLY VARIATIONS IN THE INFLOW OF THE AQUEOUS HUMOUR. *Acta Ophthalmologica* **36**, 381–385 (1958).
17. Wilensky, J. T. *DIURNAL VARIATIONS IN INTRAOCULAR PRESSURE.*
18. Liu, J. H. *et al.* Twenty-four-hour pattern of intraocular pressure in the aging population. *Invest Ophthalmol Vis Sci* **40**, 2912–7 (1999).
19. Wang, W. W., Wang, K.-J., Tsai, C.-L. & Wang, I.-J. Study of noncontact air-puff applanation tonometry IOP measurement on irregularly-shaped corneas. in *Biomedical Imaging and Sensing Conference* vol. 10251 102511X (SPIE, 2017).
20. Sudesh, S., Moseley, M. J. & Thompson, J. R. Accuracy of Goldmann tonometry in clinical practice. *Acta Ophthalmologica* **71**, 185–188 (1993).
21. Zimmermann, M., Pitz, S., Schmidtman, I., Pfeiffer, N. & Wasielica-Poslednik, J. Tonographic effect of ocular response analyzer in comparison to Goldmann applanation tonometry. *PLoS ONE* **12**, (2017).
22. Cockburn, D. M. Tonometry. in *Clinical Procedures in Optometry* 221–237 (1991).
23. Kaushik, S. & Pandav, S. S. Ocular response analyzer. *Journal of Current Glaucoma Practice* **6**, 17–19 (2012).

24. Uysal, B. S. *et al.* Impact of dehydration and fasting on intraocular pressure and corneal biomechanics measured by the Ocular Response Analyzer. *International Ophthalmology* **38**, 451–457 (2018).
25. Joel L. Zuckerman Harry J. Grossman. Method of measuring ocular pulse.
26. Akca, B. I. *et al.* Observation of sound-induced corneal vibrational modes by optical coherence tomography. *Biomedical Optics Express* **6**, 3313 (2015).
27. Koprowski, R. & Wilczyński, S. Corneal Vibrations during Intraocular Pressure Measurement with an Air-Puff Method. *Journal of Healthcare Engineering* vol. 2018 Preprint at <https://doi.org/10.1155/2018/5705749> (2018).
28. Grolman, B. A new tonometer system. *Optometry and Vision Science* **49.8**, 646–660 (1972).
29. McLaren, J. W., Brubaker, R. F. & Fitzsimon, ] Susan. *Continuous Measurement of Intraocular Pressure in Rabbits by Telemetry*.
30. Kakaday, T., Hewitt, A. W., Voelcker, N. H., Li, J. S. J. & Craig, J. E. Advances in telemetric continuous intraocular pressure assessment. *British Journal of Ophthalmology* vol. 93 992–996 Preprint at <https://doi.org/10.1136/bjo.2008.144261> (2009).
31. Hernández-Verdejo, J. L., Teus, M. A. & Bolivar, G. Simultaneous measurement of intraocular pressure in the anterior chamber and the vitreous cavity. *Acta Ophthalmologica* vol. 88 Preprint at <https://doi.org/10.1111/j.1755-3768.2009.01751.x> (2010).
32. Mansouri, K. & Shaarawy, T. Continuous intraocular pressure monitoring with a wireless ocular telemetry sensor: Initial clinical experience in patients with open angle glaucoma. *British Journal of Ophthalmology* **95**, 627–629 (2011).
33. Pirani, P. *Contact lens tonometry-Application in humans Optical Bistability in Prism Couplers View project Dynamic contour tonometry View project Hartmut Kanngiesseer Independent Researcher*. <https://www.researchgate.net/publication/13853529> (1997).
34. Mottet, B. *et al.* 24-hour intraocular pressure rhythm in young healthy subjects evaluated with continuous monitoring using a contact lens sensor. *JAMA Ophthalmology* **131**, 1507–1516 (2013).
35. Lorenz, K. *et al.* Tolerability of 24-hour intraocular pressure monitoring of a pressure-sensitive contact lens. *Journal of Glaucoma* **22**, 311–316 (2013).
36. Mansouri, K., Liu, J. H. K., Weinreb, R. N., Tafreshi, A. & Medeiros, F. A. Analysis of continuous 24-hour intraocular pressure patterns in glaucoma. *Investigative Ophthalmology and Visual Science* **53**, 8050–8056 (2012).
37. Mansouri, K., Medeiros, F. A., Tafreshi, A. & Weinreb, R. N. Continuous 24-hour monitoring of intraocular pressure patterns with contact lens sensor: Safety, tolerability, and reproducibility in patients with glaucoma. *Archives of Ophthalmology* **130**, 1534–1539 (2012).
38. Yosef Mandellsmail E Araci Stephen R. Quake. Implantable Micro-Fluidic Device for Monitoring of Intra-Ocular Pressure.
39. de Smedt, S., Mermoud, A. & Schnyder, C. 24-hour intraocular pressure fluctuation monitoring using an ocular telemetry sensor: Tolerability and functionality in healthy subjects. *Journal of Glaucoma* **21**, 539–544 (2012).

40. Torre-Ibarra, M. H. D. la, Ruiz, P. D. & Huntley, J. M. Double-shot depth-resolved displacement field measurement using phase-contrast spectral optical coherence tomography. *Optics Express* **14**, 9643 (2006).
41. Matsumoto, T., Nagata, R., Saishin, M., Matsuda, T. & Nakao, S. *Measurement by holographic interferometry of the deformation of the eye accompanying changes in intraocular pressure*. *APPLIED OPTICS* vol. 17.
42. Asejczyk-Widlicka, M. & Pierscionek, B. K. Fluctuations in intraocular pressure and the potential effect on aberrations of the eye. *British Journal of Ophthalmology* **91**, 1054–1058 (2007).
43. Dubois, P. *et al.* A New Method for Intra Ocular Pressure in vivo Measurement: First Clinical Trials. in *2007 29th Annual International Conference of the IEEE Engineering in Medicine and Biology Society* 5762–5765 (IEEE, 2007). doi:10.1109/IEMBS.2007.4353656.
44. Zalevsky, Z. *et al.* Simultaneous remote extraction of multiple speech sources and heart beats from secondary speckles pattern. *Optics Express* **17**, 21566 (2009).
45. Beiderman, Y. *et al.* Remote estimation of blood pulse pressure via temporal tracking of reflected secondary speckles pattern. *Journal of Biomedical Optics* **15**, 061707 (2010).
46. Ozana, N. *et al.* Demonstration of a Remote Optical Measurement Configuration That Correlates with Breathing, Heart Rate, Pulse Pressure, Blood Coagulation, and Blood Oxygenation. *Proceedings of the IEEE* **103**, 248–262 (2015).
47. Kalyuzhner, Z., Agdarov, S., Bennett, A., Beiderman, Y. & Zalevsky, Z. Remote photonic sensing of blood oxygen saturation via tracking of anomalies in micro-saccades patterns. *Optics Express* **29**, 3386 (2021).
48. Kalyuzhner, Z. *et al.* Remote photonic detection of human senses using secondary speckle patterns. *Scientific Reports* **12**, (2022).
49. Kalyzhner, Z., Levitas, O., Kalichman, F., Jacobson, R. & Zalevsky, Z. Photonic human identification based on deep learning of back scattered laser speckle patterns. *Optics Express* **27**, 36002 (2019).
50. Bennett, A. *et al.* Intraocular pressure remote photonic biomonitoring based on temporally encoded external sound wave stimulation. *Journal of Biomedical Optics* **23**, 1 (2018).
51. Ruiz-Ederra, J. *et al.* The pig eye as a novel model of glaucoma. *Experimental Eye Research* **81**, 561–569 (2005).
52. Camacho-Lopez, S. *et al.* Intraocular Pressure Study in Ex Vivo Pig Eyes by the Laser-Induced Cavitation Technique: Toward a Non-Contact Intraocular Pressure Sensor. *Applied Sciences* **10**, 2281 (2020).
53. Middleton, S. Porcine Ophthalmology. *Veterinary Clinics of North America: Food Animal Practice* **26**, 557–572 (2010).
54. Tan, J., Foster, L. J. R., Lovicu, F. J. & Watson, S. L. Laser-Activated Corneal Adhesive: Retinal Safety in Rabbit Model. *Translational Vision Science & Technology* **10**, 27 (2021).
55. Harrington, P. de B., Urbas, A. & Tandler, P. J. Two-dimensional correlation analysis. *Chemometrics and Intelligent Laboratory Systems* **50**, 149–174 (2000).
56. Ghanem, B., Thabet, A., Nibbles, J. C. & Heilbron, F. C. Robust Manhattan Frame estimation from a single RGB-D image. in *2015 IEEE Conference on Computer Vision*

- and Pattern Recognition (CVPR)* 3772–3780 (IEEE, 2015).  
doi:10.1109/CVPR.2015.7299001.
57. Li, D., Zhang, J., Zhang, Q. & Wei, X. Classification of ECG signals based on 1D convolution neural network. in *2017 IEEE 19th International Conference on e-Health Networking, Applications and Services (Healthcom)* 1–6 (IEEE, 2017).  
doi:10.1109/HealthCom.2017.8210784.
  58. Santurkar, S., Tsipras, D., Ilyas, A. & Madry, A. How Does Batch Normalization Help Optimization? (2018).
  59. Agarap, A. F. M. Deep Learning using Rectified Linear Units (ReLU). *arXiv* 2–8 (2018).
  60. Wu, H. & Gu, X. Max-pooling dropout for regularization of convolutional neural networks. *Lecture Notes in Computer Science (including subseries Lecture Notes in Artificial Intelligence and Lecture Notes in Bioinformatics)* **9489**, 46–54 (2015).
  61. Li, Z. *et al.* Teeth category classification via seven-layer deep convolutional neural network with max pooling and global average pooling. *International Journal of Imaging Systems and Technology* **29**, 577–583 (2019).
  62. Wang, M., Lu, S., Zhu, D., Lin, J. & Wang, Z. A High-Speed and Low-Complexity Architecture for Softmax Function in Deep Learning. in *2018 IEEE Asia Pacific Conference on Circuits and Systems (APCCAS)* 223–226 (IEEE, 2018).  
doi:10.1109/APCCAS.2018.8605654.
  63. Zhang, Z. & Sabuncu, M. R. Generalized cross entropy loss for training deep neural networks with noisy labels. *Advances in Neural Information Processing Systems* **2018-Decem**, 8778–8788 (2018).
  64. Kingma, D. P. & Ba, J. L. Adam: A method for stochastic optimization. *3rd International Conference on Learning Representations, ICLR 2015 - Conference Track Proceedings* 1–15 (2015).
  65. Zeiler, M. D. ADADELTA: An Adaptive Learning Rate Method. (2012).

## Tables

Method		IOP range (mm Hg)	Precision (%)	Recall (%)	F1 (%)	Accuracy (%)	
Generic photonic IOP classification (without calibration or prior knowledge)		10-21	98	97	97	<b>91</b>	
		22-33	81	84	82		
		34-45	72	70	71		
Individual eye IOP classification	5 mm Hg IOP range	10-15	85	74	79	<b>80</b>	
		16-21	77	87	81		
	3 mm Hg IOP range	10-13	87	82	84	<b>83</b>	
		14-17	78	76	76		
		18-21	85	91	87		
	1 mm Hg IOP range	10-11	82	79	80	<b>70</b>	
		12-13	64	69	65		
		14-15	66	58	60		
		16-17	63	55	55		
		18-19	69	76	70		
			20-21	86	78	79	

Table 1. Generic and individual components of IOP monitoring model classification results.

The generic method, which classifies pig eyeballs without calibration or prior knowledge, attains an accuracy of 95% while maintaining a high recall of 97% and high precision of 98% in the normal IOP range classification task. The individual eye component is divided into three IOP sensitivity ranges - 5 mm Hg, 3 mm Hg, and 1 mm Hg. The 5 mm Hg range attains an accuracy of 80% while maintaining a high recall of 87% for the 16-21 mm Hg range, and 85% precision for the 10-15 mm Hg range. The 3 mm Hg range attains an accuracy of 83% while maintaining a high precision of 87% for the 10-13 mm Hg range, and 91% recall for the 18-21 mm Hg range. The 1 mm Hg range attains an accuracy of 70% while maintaining a high precision of 82% for the 10-11 mm Hg range, and 86% precision for the 20-21 mm Hg range.

## Figure legends

Figure 1. IOP biomonitoring system design. (a) A green laser with a wavelength of 532 nm is positioned directly opposite the illuminated area of the cornea, close to the pupil, to cover a 3 mm diameter area. The speckle patterns reflected from the cornea are captured using a digital camera with a frame rate of 1,000 frames per second (FPS) and spatial resolution of 64x64 pixels per frame. The camera has a 55 mm focal length and an F-number of 2.8. The camera is focused on the far field, which defocuses the cornea and speckle pattern. A high-fidelity loudspeaker (Pioneer Ts-G1615R) with an excitation frequency of 390Hz@105dB is used to stimulate the cornea. (b) A 532 nm green laser illuminates the sclera of a pig, while a Basler AcaA1300-200um area scan camera with defocused optics captures the speckle patterns that are reflected. The IOP of the pig eye sample is regulated by inserting a needle behind the eye. The needle is attached to a calibrated burette containing water. The source of the sound wave agitating the sclera is connected to the frequency generator. Using a MATLAB-based application, a computer refines the video files captured by the camera.

Figure 2. Confusion matrices of IOP trained models. (a) Trained generic model confusion matrix and 100-millisecond data sample of a pre-processed speckle pattern signal from a single tested eye. According to the confusion matrix, the average IOP range detection of a single test sample is 97%, with a low error rate. The success rates for identifying high IOP ranges are also high, at 84% (22-33 mm Hg) and 70% (34-45 mm Hg), with almost all errors occurring between these two IOP ranges. (b) Confusion matrices of the three IOP classification tasks performed on a single eye. This demonstrates that the trained IOP classification model errors are common in close IOP ranges and do not disperse across all possible IOP ranges, indicating that the models are learning successfully. Furthermore, the confusion matrix for the 1 mm Hg IOP range

variation shows that the high error rate occurs in the middle IOP ranges rather than at the edges. These errors also have relatively low values.

Figure 3. IOP simulation and preprocessing. An injection needle was inserted into the eyeball and connected to a calibrated burette filled with water by means of a flexible pipe to simulate IOP. Each 1 mm Hg was thought to be equivalent to a 13.2 mm water column. Each eye was tested under a single needle penetration and the IOP was increased in steps of 1 mm Hg in the range of 10-45 mm Hg. Each video, including 52,000 frames, was pre-processed for frame correlation extraction in order to classify the IOP. For each pair of consecutive frames, the correlation was computed using a fully discrete 2-dimensional linear cross-correlation with symmetrical boundary conditions to reflect the difference between the two frames. This signal difference was adjusted using the Manhattan norm.

Figure 4. DNN model architecture and feature extraction sample. (a) DNN model architecture. We can understand the behavior of our model's decision-making process by extracting our trained convolutional layer filters and displaying them on a new input signal. (b) The input signal had a duration of 25,000 milliseconds and was normalized to represent 26 consecutive cycles in the 0-1 range. Furthermore, our trained 64 convolutional layer filters constituted the DNN's final convolutional layer, with their amplitude expressing the decision's confidence level when 1 is highest and 0 is lowest. Filters with amplitudes less than 0.8 were used after filtering layers. (c) When the eyeball started or stopped reacting to the sound of the external stimulation signal, defined by a vibratory change in the eye, the DNN classified the IOP level. Each IOP level involved a change in the weight, volume, and geometry of the eye, which had a direct impact on the shape, direction, and speed of eye movement, all of which were influenced by the sound signal. It is possible to conclude from this physiological explanation that the IOP level of the eye can be determined by remotely sensing nano-vibrations of the eye caused by an external sound signal.

# Figures

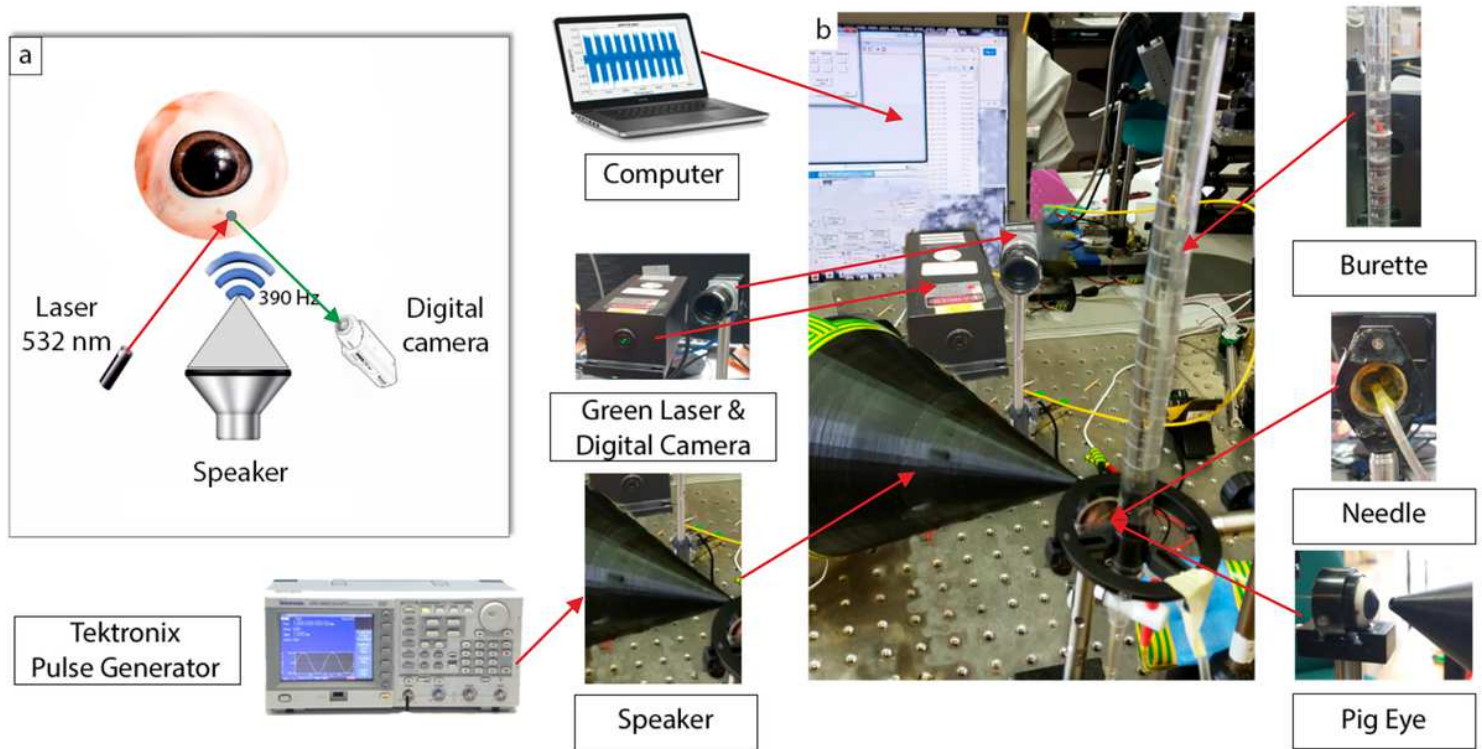


**Figure 1**

IOP biomonitoring system design. (a) A green laser with a wavelength of 532 nm is positioned directly opposite the illuminated area of the cornea, close to the pupil, to cover a 3 mm diameter area. The speckle patterns reflected from the cornea are captured using a digital camera with a frame rate of 1,000 frames per second (FPS) and spatial resolution of 64x64 pixels per frame. The camera has a 55 mm focal length and an F-number of 2.8. The camera is focused on the far field, which defocuses the cornea and speckle pattern. A high-fidelity loudspeaker (Pioneer Ts-G1615R) with an excitation frequency of 390Hz@105dB is used to stimulate the cornea. (b) A 532 nm green laser illuminates the sclera of a pig, while a Basler AcaA1300-200um area scan camera with defocused optics captures the speckle patterns that are reflected. The IOP of the pig eye sample is regulated by inserting a needle behind the eye. The needle is attached to a calibrated burette containing water. The source of the sound wave agitating the sclera is connected to the frequency generator. Using a MATLAB-based application, a computer refines the video files captured by the camera.

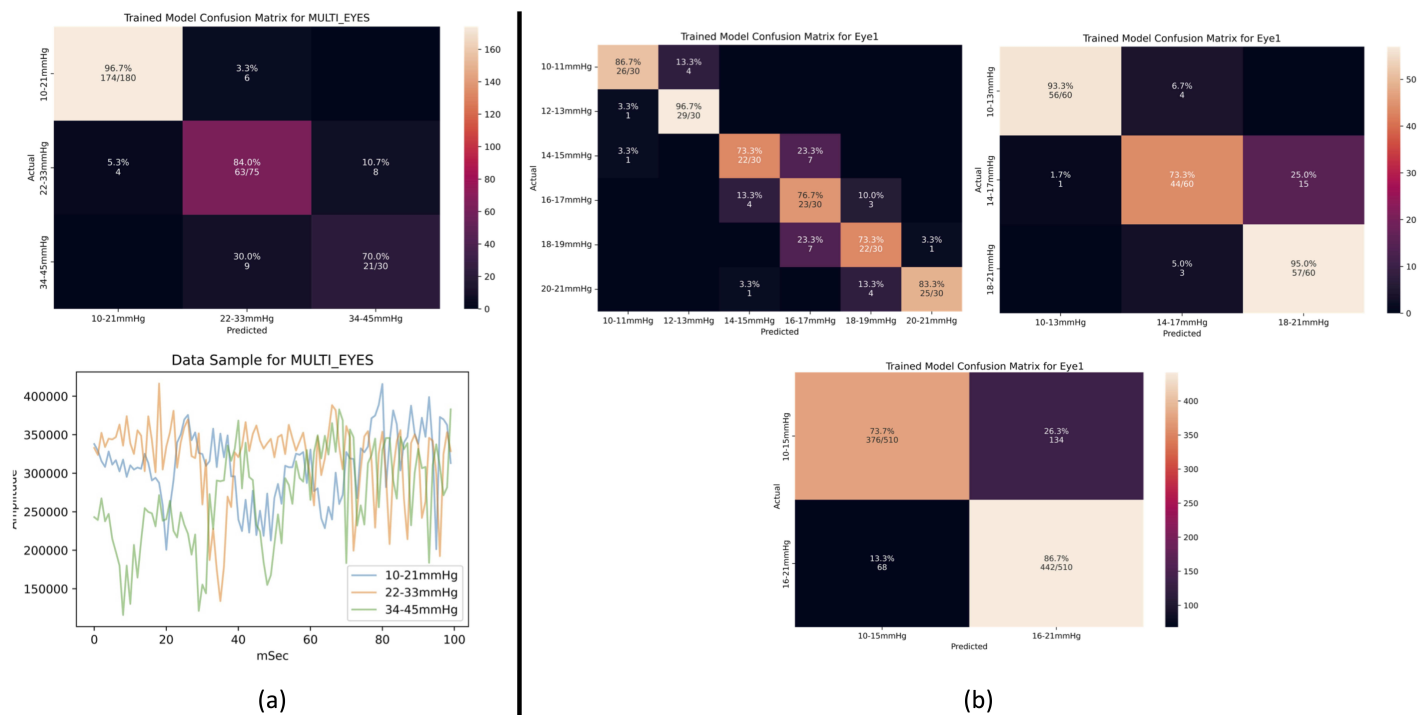


**Figure 2**

Confusion matrices of IOP trained models. (a) Trained generic model confusion matrix and 100-millisecond data sample of a pre-processed speckle pattern signal from a single tested eye. According to the confusion matrix, the average IOP range detection of a single test sample is 97%, with a low error rate. The success rates for identifying high IOP ranges are also high, at 84% (22-33 mm Hg) and 70% (34-45 mm Hg), with almost all errors occurring between these two IOP ranges. (b) Confusion matrices of the three IOP classification tasks performed on a single eye. This demonstrates that the trained IOP classification model errors are common in close IOP ranges and do not disperse across all possible IOP ranges, indicating that the models are learning successfully. Furthermore, the confusion matrix for the 1 mm Hg IOP range variation shows that the high error rate occurs in the middle IOP ranges rather than at the edges. These errors also have relatively low values.

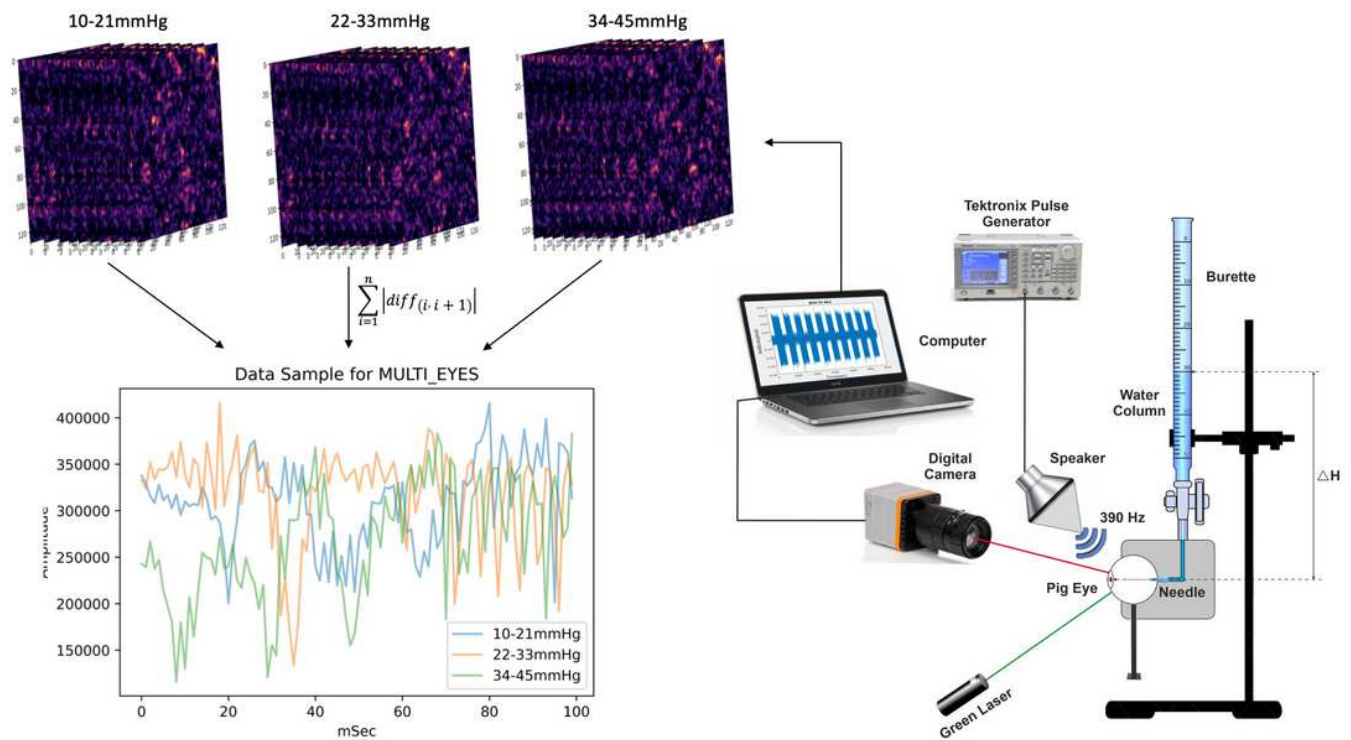


**Figure 3**

IOP simulation and preprocessing. An injection needle was inserted into the eyeball and connected to a calibrated burette filled with water by means of a flexible pipe to simulate IOP. Each 1 mm Hg was thought to be equivalent to a 13.2 mm water column. Each eye was tested under a single needle penetration and the IOP was increased in steps of 1 mm Hg in the range of 10-45 mm Hg. Each video, including 52,000 frames, was pre-processed for frame correlation extraction in order to classify the IOP. For each pair of consecutive frames, the correlation was computed using a fully discrete 2-dimensional linear cross-correlation with symmetrical boundary conditions to reflect the difference between the two frames. This signal difference was adjusted using the Manhattan norm.

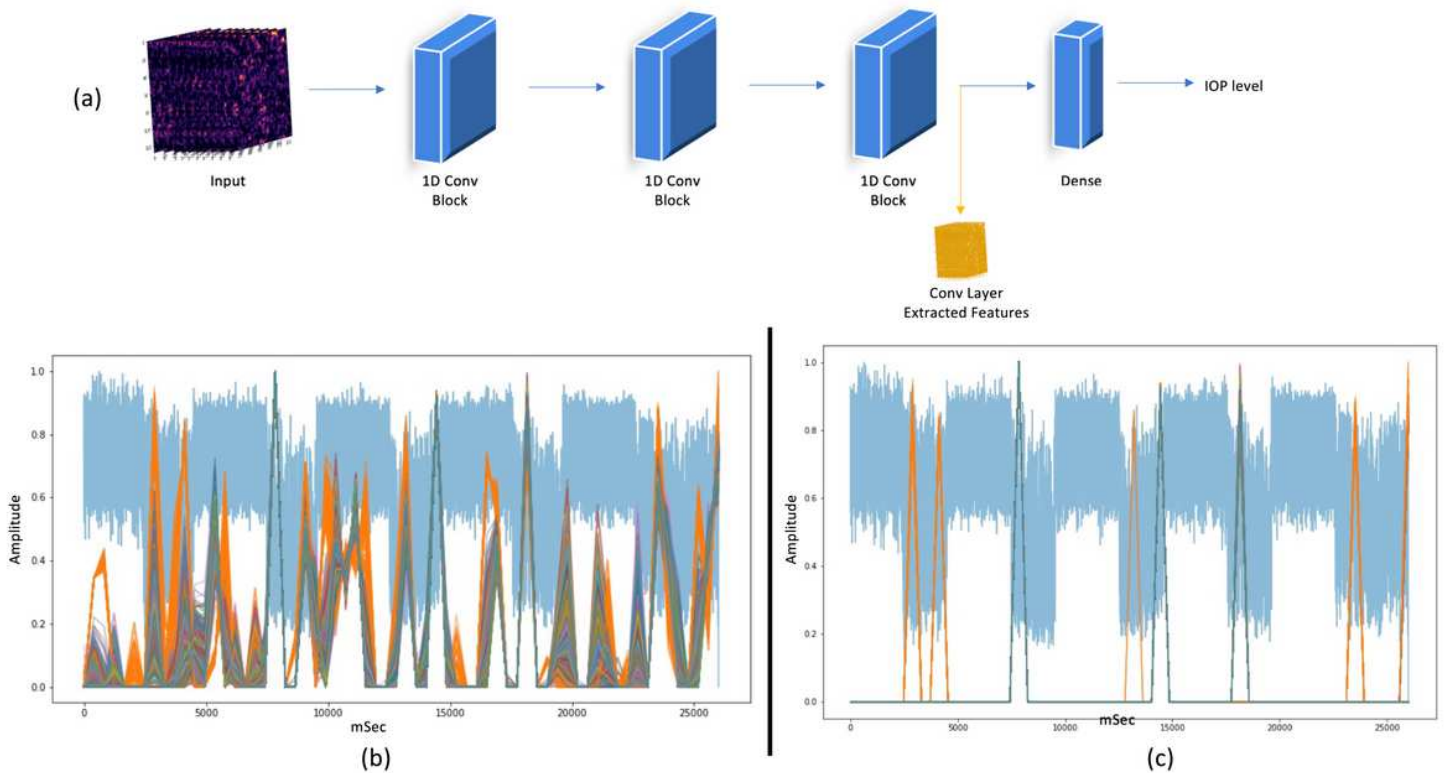


**Figure 4**

DNN model architecture and feature extraction sample. (a) DNN model architecture. We can understand the behavior of our model's decision-making process by extracting our trained convolutional layer filters and displaying them on a new input signal. (b) The input signal had a duration of 25,000 milliseconds and was normalized to represent 26 consecutive cycles in the 0-1 range. Furthermore, our trained 64 convolutional layer filters constituted the DNN's final convolutional layer, with their amplitude expressing the decision's confidence level when 1 is highest and 0 is lowest. Filters with amplitudes less than 0.8 were used after filtering layers. (c) When the eyeball started or stopped reacting to the sound of the external stimulation signal, defined by a vibratory change in the eye, the DNN classified the IOP level. Each IOP level involved a change in the weight, volume, and geometry of the eye, which had a direct impact on the shape, direction, and speed of eye movement, all of which were influenced by the sound signal. It is possible to conclude from this physiological explanation that the IOP level of the eye can be determined by remotely sensing nano-vibrations of the eye caused by an external sound signal.